## **PHOTONICS**

# Ultrafast mode-locked laser in nanophotonic lithium niobate

Qiushi Guo<sup>1,2,3</sup>\*, Benjamin K. Gutierrez<sup>4</sup>, Ryoto Sekine<sup>1</sup>, Robert M. Gray<sup>1</sup>, James A. Williams<sup>1</sup>, Luis Ledezma<sup>1,5</sup>, Luis Costa<sup>1</sup>, Arkadev Roy<sup>1</sup>, Selina Zhou<sup>1</sup>, Mingchen Liu<sup>1</sup>, Alireza Marandi<sup>1,4</sup>\*

Mode-locked lasers (MLLs) generate ultrashort pulses with peak powers substantially exceeding their average powers. However, integrated MLLs that drive ultrafast nanophotonic circuits have remained elusive because of their typically low peak powers, lack of controllability, and challenges when integrating with nanophotonic platforms. In this work, we demonstrate an electrically pumped actively MLL in nanophotonic lithium niobate based on its hybrid integration with a III-V semiconductor optical amplifier. Our MLL generates ~4.8-ps optical pulses around 1065 nm at a repetition rate of ~10 GHz, with energies exceeding 2.6 pJ and peak powers beyond 0.5 W. The repetition rate and the carrier-envelope offset frequency of the output can be controlled in a wide range by using the driving frequency and the pump current, providing a route for fully stabilized on-chip frequency combs.

ode-locked lasers (MLLs), which generate intense and coherent ultrashort optical pulses on picosecond and femtosecond timescales, have enabled numerous sciences and technologies in photonics such as extreme nonlinear optics (1), supercontinuum generation (2), optical atomic clocks (3), optical frequency combs (4), biological imaging (5), and photonic computing (6). Today's state-of-the-art MLLs are based on discrete fiberbased and free-space optical components and

are expensive, power demanding, and bulky. Realizing MLLs on integrated photonic platforms promises widespread use of ultrafast photonic systems that are currently limited to table-top laboratory experiments. However, the performance of integrated MLLs has not been on par with their table-top counterparts, lacking the required peak intensities and degrees of controllability required for on-chip ultrafast optical systems (7). A major challenge lies in the simultaneous realization of large

laser gain and an efficient mode-locking manism on integrated photonic platforms. though III-V semiconductor gain media can be electrically pumped and exhibit a very high gain per unit length and high saturation powers (8), the conventional method of achieving mode-locking and short pulse generation on the same semiconductor chip requires a narrow range of pumping current, thus substantially limiting the output power and the tunability of the integrated MLLs (9, 10).

To realize high-peak-power integrated MLLs, a promising approach consists of the hybrid integration of a semiconductor gain medium and an external mode-locking element based on electrooptic (EO) or nonlinear optical effects. Thin-film lithium niobate (TFLN) has emerged as a promising integrated nonlinear photonic platform with access to power-efficient and high-speed EO modulation (11, 12) and strong quadratic [ $\chi^{(2)}$ ] optical nonlinearity (13, 14).

<sup>1</sup>Department of Electrical Engineering, California Institute of Technology, Pasadena, CA, USA. <sup>2</sup>Photonics Initiative, Advanced Science Research Center, City University of New York, NY, USA. <sup>3</sup>Physics Program, Graduate Center, City University of New York, New York, NY, USA. <sup>4</sup>Department of Applied Physics, California Institute of Technology, Pasadena, CA, USA. <sup>5</sup>Jet Propulsion Laboratory, Pasadena, CA, USA.

\*Corresponding author. Email: qguo@gc.cuny.edu (Q.G.); marandi@caltech.edu (A.M.)

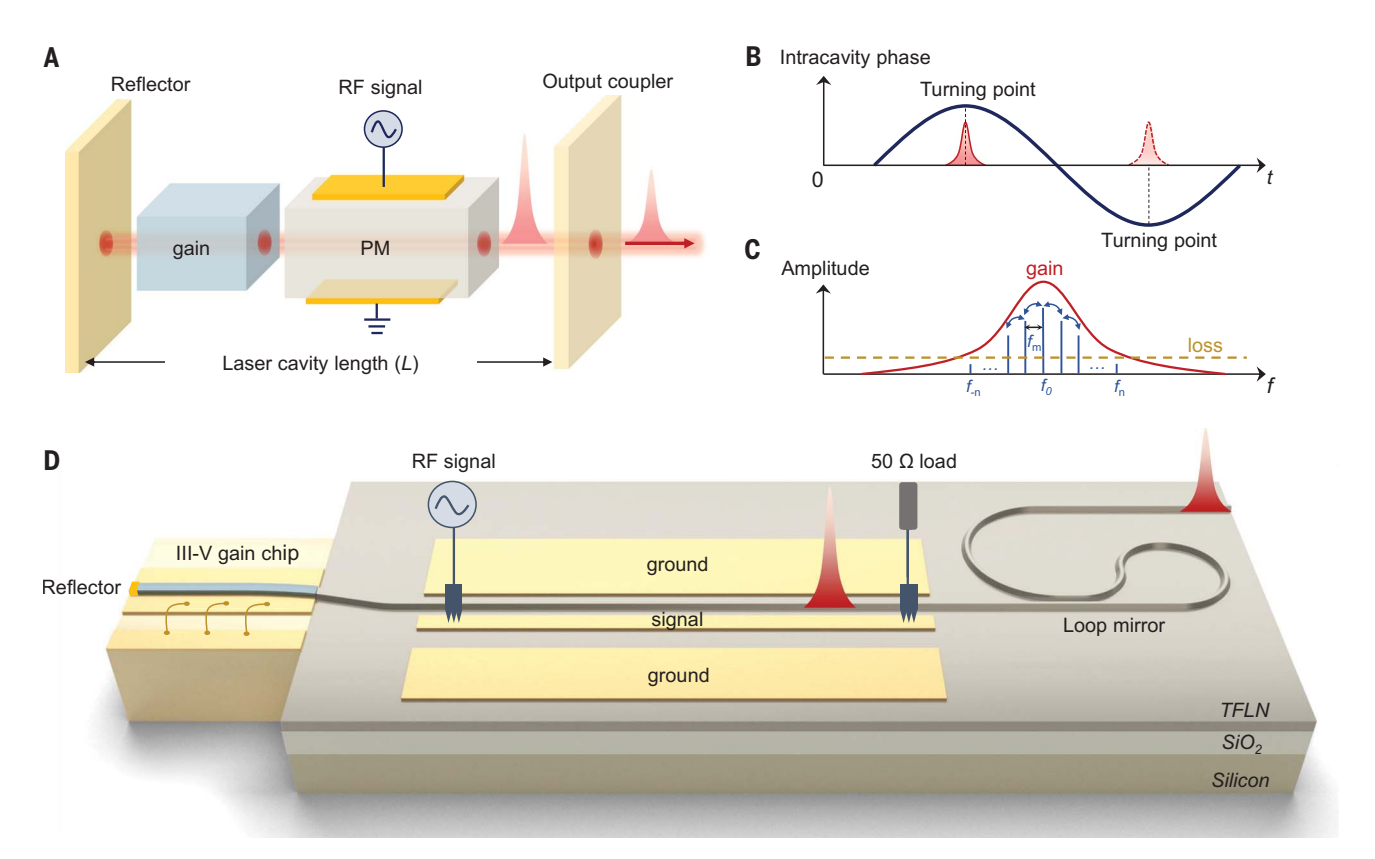


Fig. 1. Principle and design of integrated actively MLL laser. (A) Diagram of active mode-locking through intracavity phase modulation. (B) Illustration of mode-locking in the time domain. (C) Illustration of mode-locking in the frequency domain. (D) Schematic of the integrated actively MLL.

Hybrid integration of semiconductor gain with TFLN enables a strong interplay between the laser gain and the EO or nonlinear effects to achieve active or passive mode-locking with high efficiency and tunability. Moreover, many of the nonlinear and ultrafast optical functionalities such as supercontinuum generation (15), optical parametric oscillation (16-18), pulse shortening (19), all-optical switching (20), and quantum squeezing (21) can be realized in quasi-phase-matched LN nanophotonic devices with orders-of-magnitude lower peak powers compared with other platforms. Therefore, developing high-peak-power MLLs integrated into nanophotonic LN can enable a suite of nonlinear and ultrafast optical phenomena on a chip, promising integrated photonic systems with unprecedented performance and functionalities. In this work, we demonstrate a high-peak-power, electrically pumped, integrated, actively MLL by hybrid integration of III-V semiconductors and LN nanophotonics. Our MLL exploits the high laser gain of III-V semiconductors and the efficient active optical phase modulation in LN nanophotonic waveguides as the mode-locking mechanism. Such a design eliminates the complexities associated with realizing gain and saturable absorption on the same semiconductor chip, allowing a much

higher output power and a wider tunability of the laser.

## Mode-locked laser operating principle and design

Figure 1A shows the concept of active modelocking by intracavity EO phase modulation. In the time domain, when a phase modulator (PM) is driven by a sinusoidal radio frequency (RF) signal at a frequency  $f_{\rm m}$ , the intracavity phase modulation is equivalent to the cavity length modulation. Therefore, the laser cavity can be considered as having a moving end mirror with a sinusoidal motion at frequency  $f_{\rm m}$ . When an optical signal inside the cavity strikes this moving end mirror and gets reflected back. its optical frequency acquires a Doppler shift. After successive round trips, these Doppler shifts will accumulate, resulting in no steadystate solution. However, when a short circulating pulse strikes the end mirror at either of the "turning points" where the mirror reverses its direction (the extremum of the phase variation as shown in Fig. 1B), it will not acquire a Doppler frequency shift, but instead, a small quadratic phase modulation or chirp (22). Thus, a steady-state optical pulse can be maintained in the laser cavity after successive round trips. Although in principle, optical pulses can occur at either of the two phase modulation extrema and acquire chirps of different signs, the dispersion in the cavity can compensate for the chirp imposed by the PM at one extremum, and further chirp the pulse formed at another extremum (23). The mode-locking mechanism can also be understood in the frequency domain (Fig. 1C). When the intracavity phase modulation frequency  $f_{\rm m}$  matches the cavity free spectral range (FSR), the sidebands produced by each of the running axial modes are injected into the adjacent axial modes, resulting in the phase locking of adjacent modes. Notably, in MLLs, these modes will lase because of the presence of laser gain within the cavity, whereas in EO comb sources, they are generated by dispersing the energy from a single pump laser line (24-27).

Figure 1D shows the design of our integrated MLL based on this principle. In our MLL, an electrically pumped single-angled facet (SAF) GaAs gain chip is butt-coupled to a TFLN chip that contains an integrated EO PM and a broadband loop mirror. A Fabry-Perot laser cavity configuration is formed between the reflective facet on the left end of the SAF gain chip and the broadband loop mirror on the TFLN chip. Here, an integrated PM is preferred over a Mach Zehnder interferometer (MZI)-

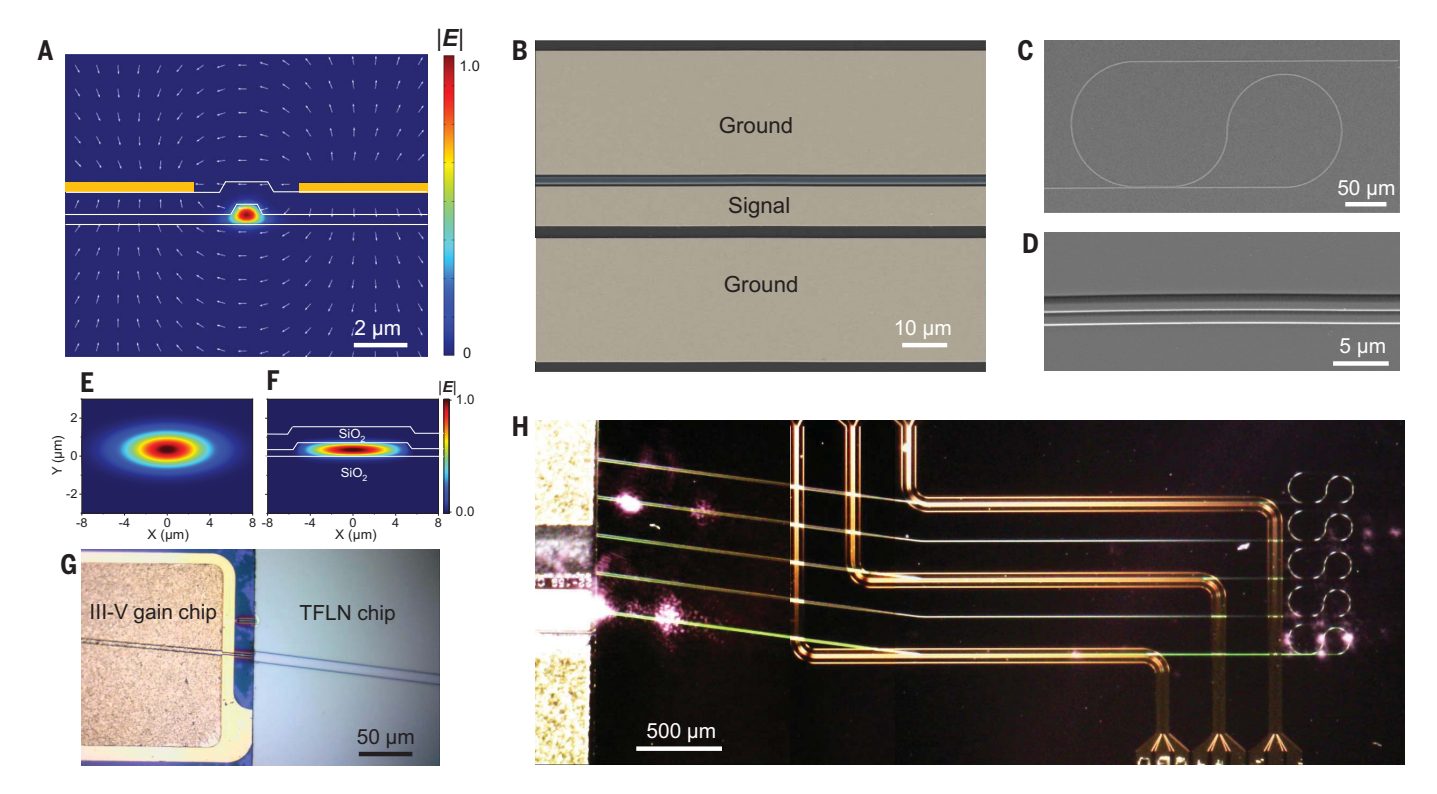
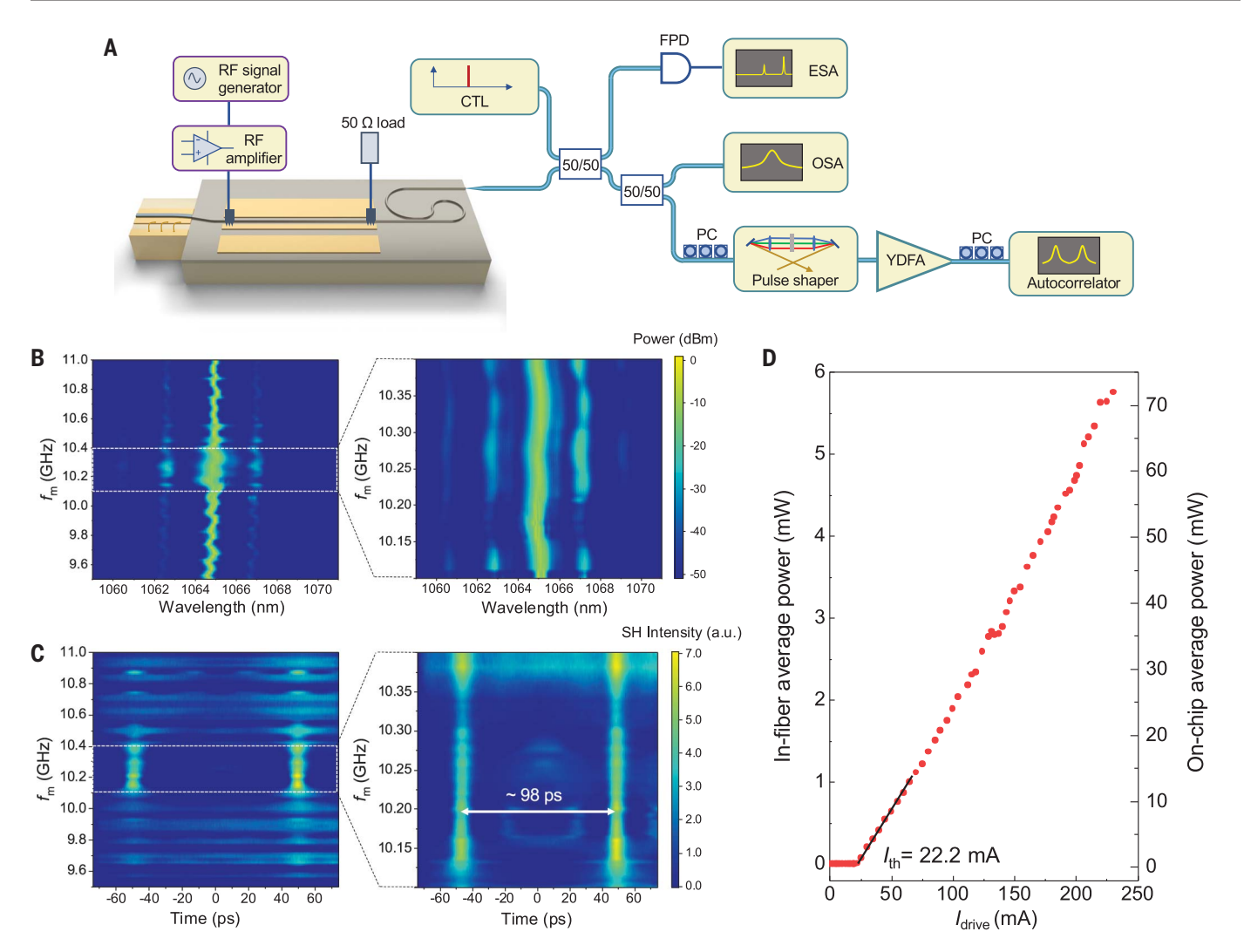


Fig. 2. Integrated actively MLL laser on TFLN. (A) Cross-sectional view of the PM region and the distribution of microwave field (white arrows) at 10 GHz and the optical field of the fundamental TE mode (color map) at 1065 nm. The RF electrodes are marked in vellow. |E|, normalized electric field. (B) False-colored SEM image of the PM region in the fabricated device. The RF electrodes are marked in yellow and the optical waveguide is

marked in blue. (C) SEM image of the broadband loop mirror. (D) The curved coupling region of the broadband loop mirror. (E and F) The fundamental TE mode profile at 1065 nm in both the (E) SAF gain chip waveguide and (F) TFLN waveguide taper. (G) Optical microscope image showing the coupling region between the two chips.

(H) Dark-field optical microscope image of the integrated MLL when operating.



**Fig. 3.** Characterization of integrated actively MLL. (A) Schematic of the experimental setup. CTL, continuously tunable CW laser; FPD, fast photodetector; OSA, optical spectrum analyzer; ESA, electrical spectrum analyzer; YDFA, ytterbium-doped fiber amplifier. (B) The optical

spectrum of the MLL output as a function of the RF driving frequency  $f_{\rm m}.$ 

- (C) Intensity autocorrelation of the MLL output as a function of the  $f_{\rm m}$ .
- (**D**) Laser average output power versus  $I_{\text{drive}}$  when  $f_{\text{m}}$  = 10.17 GHz.  $I_{\text{th}}$ , threshold driving current.

based intensity modulator (IM) because the PM offers a lower insertion loss and avoids effects from the dc bias drift of the MZI modulator (28). For the PM, we used an RF coplanar waveguide (CPW) design with ground-signal-ground (GSG) configuration to ensure the transmission of the RF wave with minimal radiative loss.

## Characterization of mode-locked lasers

We fabricated our devices on a 700-nm-thick X-cut magnesium oxide (MgO)-doped TFLN on a SiO<sub>2</sub>/Si substrate. In the PM region (Fig. 2A), the RF CPW was fabricated on top of the SiO<sub>2</sub> cladding layer. Such a design allowed us to achieve high modulation efficiency (simulated  $V_{\pi}L=1.1$  V·cm) by having a small gap (4  $\mu$ m here) between the ground and signal electrodes and a significant overlap between the RF field and the optical field in the waveguide (12, 29). We designed the geometry of the RF CPW to

ensure a 50- $\Omega$  impedance around 10 GHz. Figure 2, B to D, shows the scanning electron microscope (SEM) images of the fabricated PM and the loop mirror. We adopted a curved coupling-region design in the loop mirror to ensure broadband reflection (see supplementary materials section I for details). Based on the length (1.5 mm) and the refractive index of the SAF gain chip around 1065 nm, we estimate that a ~3-mm-long TFLN waveguide including the loop mirror section can lead to a laser cavity FSR of ~10 GHz.

Figure 2E shows the 1065-nm fundamental transverse electric (TE)-mode profile in the waveguide of the SAF gain chip. To minimize the coupling loss between the SAF gain chip and the TFLN chip, the top width of the input facet of the TFLN waveguide was tapered out to be 10.3  $\mu$ m. The 1065-nm fundamental TE-mode profile in the tapered TFLN waveguide is shown in Fig. 2F. This design ensures a maximal over-

lap with the optical mode produced by the SAF gain chip. We estimate a chip coupling loss of 3.4 to 3.9 dB in our experiments (see supplementary materials section II for details). The chip coupling loss can be further reduced by using a mode-size converter based on an inverted taper edge coupler embedded in a polvmer waveguide (30, 31). Figure 2G shows the microscope image of the chip coupling region after the alignment. When the SAF gain chip is electrically pumped with a driving current  $(I_{\rm drive})$  of 160 mA, we observed green light (the second harmonic of the 1065-nm light) inside the laser cavity (Fig. 1H), which indicated a high intracavity power around 1065 nm and a good alignment between the two chips.

We characterized the integrated actively MLL using the optical setup shown in Fig. 3A. We applied a ~280-mW sinusoidal RF signal to the left end of the CPW of the PM using the RF probe. The right end of the CPW is terminated

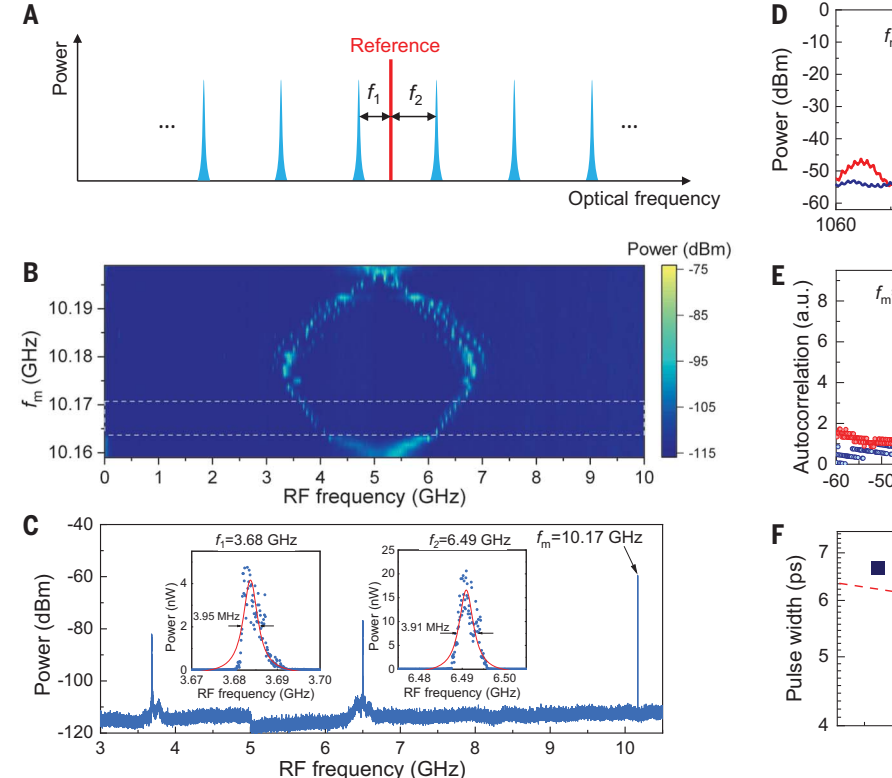
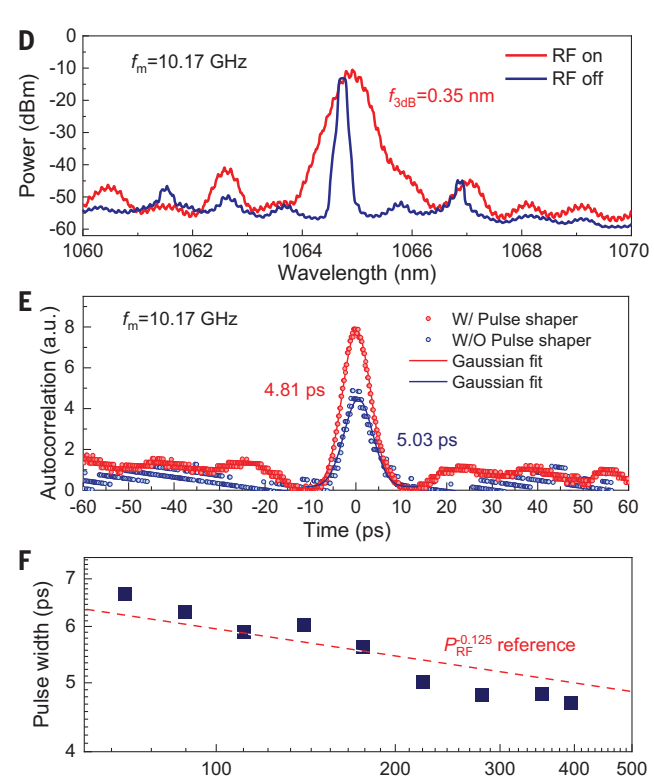


**Fig. 4. Finding the mode-locking regime of integrated MLL.** (**A**) Illustration of the generation of heterodyne beat notes. (**B**) Evolution of heterodyne beat notes with the  $f_{\rm m}$ . The mode-locking regime is marked by the white dashed box. (**C**) Heterodyne beat notes measured at  $f_{\rm m} = 10.17$  GHz. (Insets) Zoomed-in view of the two beat notes at  $f_{\rm 1} = 3.68$  GHz and  $f_{\rm 2} = 6.49$  GHz. Blue symbols represent measured data and solid red curves indicate Lorentz fits. (**D**) Output optical spectra of the MLL when the RF drive at 10.17 GHz is on (red) and off



(blue). The side lobes around 1062.7 and 1067 nm can be due to the reflections in the gap between the gain chip and the TFLN chip. The fast modulation can be due to the reflections within the gain chip. (**E**) Intensity autocorrelation traces of the MLL output measured at  $f_m = 10.17$  GHz with (red) and without (blue) the external pulse shaper. Symbols represent measurement data and solid curves indicate Gaussian fits. a.u., arbitrary units. (**F**) Dependence of pulse width on  $P_{RF}$ . The red dashed line represents the  $1/\sqrt[8]{P_{RF}}$  scaling law according to the HME.

P<sub>RF</sub> (mW)

by another RF probe with a commercially available 50- $\Omega$  load resistor. While the gain chip was pumped with an  $I_{\rm drive}$  of 185.2 mA, we simultaneously collected the laser output spectra, the intensity autocorrelation of the laser output, and the heterodyne beat notes between two neighboring laser emission lines and a narrowlinewidth (~10 kHz) reference continuous wave (CW) tunable laser. As shown in Fig. 3B, when we scanned the  $f_{\rm m}$ , the laser output exhibited a clear spectral broadening between 10.1 and 10.4 GHz (labeled by the white dashed box). Within this  $f_{\rm m}$  range, two distinct intensity autocorrelation peaks separated by ~98 ps emerged (Fig. 3C), indicating that optical pulses are formed. At an  $f_{\rm m}$  of 10.17 GHz, we measured the laser output power from the output facet of the TFLN chip. As shown in Fig. 3D, the laser exhibits a low threshold  $I_{\text{drive}}$ of 22 mA. Given the measured coupling loss of ~11 dB between the TFLN waveguide and the single-mode lensed fiber, the on-chip laser output average power is more than 50 mW when the  $I_{\rm drive}$  is greater than 180 mA.

Heterodyne beat notes were used to characterize the mode-locking and resulting fre-

quency comb. As illustrated in Fig. 4A, when the frequency of the reference CTL is resting in between the two neighboring comb lines of the MLL near the center of its spectrum, two RF beat notes at  $f_1$  and  $f_2$  are generated on the fast detector. As shown in Fig. 4B, when  $f_{\rm m}$  is between 10.165 and 10.173 GHz, as labeled by the white dashed box, two spectrally narrow beat notes are observed. This suggests that within this range of  $f_{\rm m}$ , the laser operates in the modelocked regime, producing ultrashort optical pulses with high coherence. When  $f_{\rm m}$  is slightly detuned between 10.165 and 10.173 GHz,  $f_1$  and  $f_2$  can shift significantly with  $f_{\rm m}$  (Fig. 4B). This indicates that the carrier frequency of the MLL sensitively depends on  $f_m$ . However, when the  $f_{\rm m}$  is further detuned from the cavity FSR, the MLL exhibits a transition to a turbulent regime (32), which is manifested by multiple noisy beat notes around  $f_1$  and  $f_2$  in Fig. 4B. In the turbulent regime, the laser can still emit ultrashort pulses as shown in Fig. 3C, albeit with low coherence.

As shown in Fig. 4C, at  $f_{\rm m}=10.17$  GHz, we obtained two spectrally narrow RF beat notes at  $f_1=3.68$  GHz and  $f_2=6.49$  GHz, with full

width at half maximum (FWHM) linewidths of 3.95 and 3.91 MHz, respectively. Given that the RF drive has a very small phase noise, and no active locking of the laser cavity was used here, the linewidths of the heterodyne beat notes can be mainly limited by the drift of pulse carrier frequency. As shown in Fig. 4D, when a 280-mW RF drive at 10.17 GHz was applied to the PM, significant spectral broadening was observed. The pulse spectrum was centered at 1064.9 nm and the FWHM of the spectrum was 0.35 nm. Meanwhile, the intensity autocorrelation trace (Fig. 4E) indicated that the MLL produced one strong pulse at one of the modulation turning points, whereas the other pulse was significantly suppressed. We fit the intensity autocorrelation trace with a Gaussian function becasue active mode locking produces Gaussian pulses according to the Haus master equation (HME) (33). The fitting yielded a pulse width of 4.81 ps with the external pulse shaping, and 5.03 ps without. Because the pulse shaper can compensate for the chirp on the output pulse and the additional chirp imposed by the fibers and the YDFA, we expect the output pulse width directly after the

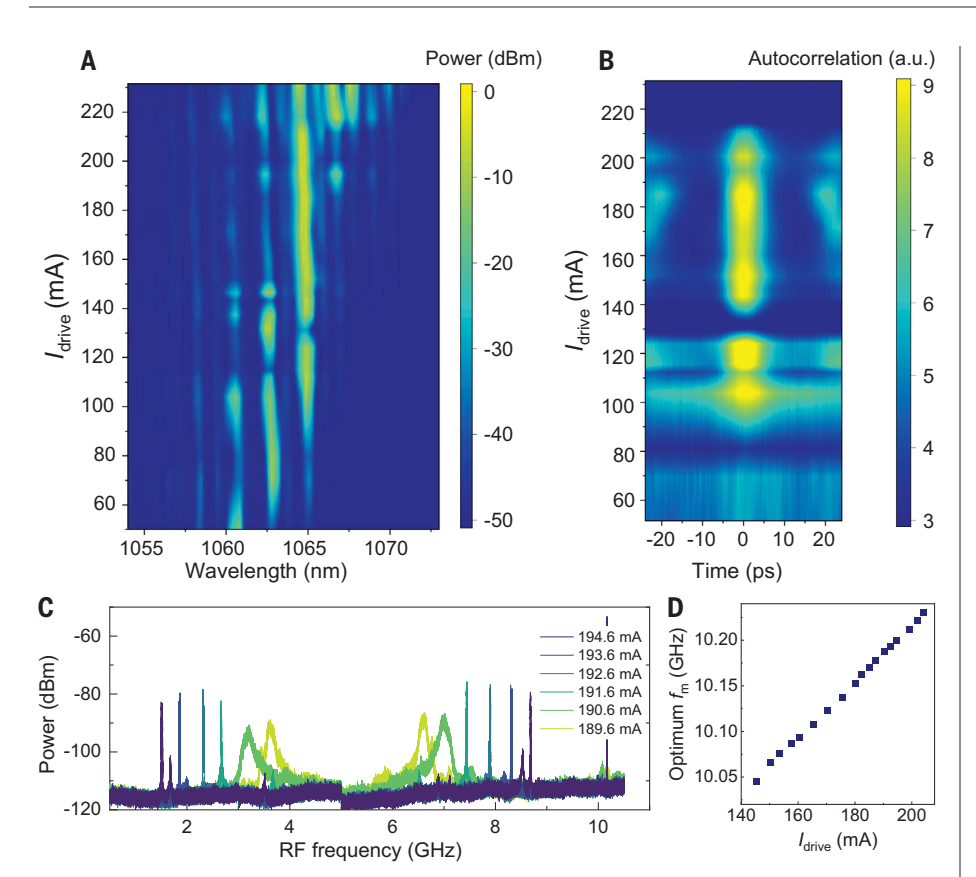


Fig. 5. Current tuning of integrated actively MLL. (A) The optical spectrum of the MLL output as a function of  $I_{drive}$ . (B) Autocorrelation trace of the MLL output as a function of  $I_{drive}$ . a.u., arbitrary units. (C) Tuning of the heterodyne beat notes by the I<sub>drive</sub>. In (A) to (C), f<sub>m</sub> is fixed at 10.18 GHz. (D) Dependence of optimum  $I_{\rm m}$  for mode-locking on  $I_{\rm drive}$ .

MLL facet to be between 4.81 ps and 5.03 ps. The pulse width of 4.81 ps after pulse shaping corresponds to a time-bandwidth product of 0.445, which is very close to the transform-limited time-bandwidth product (0.44) of a Gaussian pulse (34). To conservatively estimate the pulse energy and peak power, we used the measured output average power of 53 mW at  $I_{drive}$  = 185.2 mA and assumed that both pulses exist in the cavity. Hence, the output pulse energy of our MLL was at least 2.6 pJ and the pulse peak power was greater than 0.51 W.

We further studied the pulse width limits of our MLL. First, we found that the measured pulse only slightly decreased when the RF driving power  $P_{RF}$  was increased (Fig. 4F), which is in good agreement with the  $1/\sqrt[8]{P_{RF}}$ scaling law (red dashed line) according to the HME (35). We also found that further increasing the RF power will not shorten the pulse significantly. Instead, it can lead to laser instability due to RF heating. The HME with cavity group velocity dispersion, neglecting nonlinear effects within the laser cavity, predicts a minimum pulse width of ~2.5 ps (36). The experimentally measured pulse width was wider, likely due to several factors that are not captured by the HME such as the complex carrier dynamics and two-stage gain recovery in the III-V gain medium (37) and gain bandwidth narrowing from intracavity etalon (22) or hole burning effects (38) (see supplementary materials section IV for detailed analysis).

# **Electrical tuning of mode-locked lasers**

The  $I_{\mathrm{drive}}$  can serve as an important tuning knob of our MLL. Figure 5, A and B, shows the dependence of the output spectra and autocorrelation of the MLL on the  $I_{\text{drive}}$  with 280-mW RF drive fixed at 10.17 GHz. Within a wide range of  $I_{\rm drive}$  (140 to 205 mA), optical pulses can be formed inside the laser. In addition, the carrier frequency of the MLL blueshifted by ~0.3 nm as the  $I_{\rm drive}$  was increased from 140 to 200 mA (Fig. 5A). This was likely caused by the blueshift of the peak wavelength of the gain spectrum owing to band filling and screening effects induced by carrier injection (39). We also investigated the effect of  $I_{\text{drive}}$  on the coherence property and the  $f_{\rm rep}$  of the laser. We kept the RF drive fixed at 280 mW and 10.18 GHz. As the  $I_{\rm drive}$  was tuned from 189.6 to 194.6 mA, the laser transitioned from the turbulent to the mode-locked regime, and then back to the turbulent regime (Fig. 5C). These results suggest that, with a frequencystable reference CW laser and active feedback on  $I_{\text{drive}}$ , it may be possible to lock the carrier frequency of the MLL and operate the device as a stable frequency comb, as the repetition rate  $(f_{rep})$  of the MLL has already been locked by the external RF oscillator. As shown in Fig. 5D, when we widely varied  $I_{\rm drive}$  from 144 to 204 mA, the optimum  $f_{\rm m}$  that enables modelocking with high coherence could be varied from 10.04 to 10.23 GHz, indicating that the  $f_{\rm rep}$ of the laser could also be adjusted by ~200 MHz. Moreover, the optimum  $f_{\rm m}$  increased almost linearly with  $I_{\text{drive}}$ , which resulted from an increase of the cavity FSR caused by carrier injection in the gain medium. Although further increasing the  $I_{\rm drive}$  would not lead to laser output power saturation, we did not observe pulse formation at higher  $I_{\rm drive}$  beyond 205 mA. This is likely attributed to the significant detuning of the cavity FSR or the instability of laser mode-locking due to more pronounced self-phase modulation in the gain medium (37).

## **Conclusions and outlook**

We have demonstrated an integrated actively MLL in nanophotonic lithium niobate operating around 1065 nm, which offers the highest output pulse energy and peak power of any integrated MLLs in nanophotonic platforms (fig. S9 and table S2). Our MLL allows for a wide tuning range of the laser  $f_{rep}$  of ~200 MHz and precise control of the laser's coherence properties. The current tuning capability of our MLL indicates that active feedback to  $I_{\text{drive}}$  can achieve simultaneous locking of the carrier frequency and  $f_{\rm rep}$  of the MLL. This allows the MLL to operate as a stable frequency comb with locked carrier frequency offset ( $f_{\text{CEO}}$ ) and  $f_{\text{rep}}$ . Finally, seamless integration of our high-peak power MLL with other  $\chi^{(2)}$  nonlinear optical functionalities provided by TFLN offers opportunities for realizing new integrated photonic systems, such as fully integrated supercontinuum sources, self-referenced frequency combs, and atomic clocks.

#### REFERENCES AND NOTES

- M. Wegener, Extreme Nonlinear Optics: An Introduction (Springer Science & Business Media, 2005).
- J. M. Dudley, G. Genty, S. Coen, Rev. Mod. Phys. 78, 1135-1184
- A. D. Ludlow, M. M. Boyd, J. Ye, E. Peik, P. O. Schmidt, Rev. Mod. Phys. 87, 637-701 (2015).
- T. Udem. R. Holzwarth, T. W. Hänsch, Nature 416, 233-237 (2002)
- D. W. Piston, Trends Cell Biol. 9, 66-69 (1999).
- A. Marandi, Z. Wang, K. Takata, R. L. Byer, Y. Yamamoto, Nat. Photonics 8, 937-942 (2014).
- M. L. Davenport, S. Liu, J. E. Bowers, Photon. Res. 6, 468 (2018).
- P. J. Delfyett et al., IEEE J. Quantum Electron. 28, 2203-2219
- A. Hermans et al., APL Photonics 6, 096102 (2021).
- 10. E. Vissers et al., Opt. Express 30, 42394-42405 (2022).
- C. Wang et al., Nature 562, 101-104 (2018).
- 12. M. Xu et al., Optica 9, 61 (2022).
- 13. C. Wang et al., Optica 5, 1438 (2018).
- 14. J. Lu et al., Optica 6, 1455 (2019).
- 15. M. Jankowski et al., Optica 7, 40 (2020)

- 16. L. Ledezma et al., Sci. Adv. 9, eadf9711 (2023).
- 17. J. Lu et al., Optica 8, 539 (2021).
- 18. T. P. McKenna et al., Nat. Commun. 13, 4532 (2022).
- 19. A. Roy et al., Nat. Photonics 16, 162-168 (2022).
- 20. Q. Guo et al., Nat. Photonics 16, 625-631 (2022).
- 21. R. Nehra et al., Science 377, 1333-1337 (2022).
- D. Kuizenga, A. Siegman, *IEEE J. Quantum Electron.* 6, 694–708 (1970).
- 23. R. Nagar, D. Abraham, G. Eisenstein, *Opt. Lett.* **17**, 1119–1121 (1992).
- 24. M. Zhang et al., Nature 568, 373-377 (2019).
- 25. M. Yu et al., Nature 612, 252-258 (2022).
- 26. Y. Hu et al., Nat. Photonics 16, 679-685 (2022).
- A. Rueda, F. Sedlmeir, M. Kumari, G. Leuchs, H. G. L. Schwefel, Nature 568, 378–381 (2019).
- J. P. Salvestrini, L. Guilbert, M. Fontana, M. Abarkan, S. Gille, J. Lightwave Technol. 29, 1522–1534 (2011).
- M. Jin, J. Chen, Y. Sua, P. Kumar, Y. Huang, Opt. Lett. 46, 1884–1887 (2021).
- 30. C. Hu et al., Opt. Express 29, 5397-5406 (2021).
- E. Vissers, S. Poelman, C. O. de Beeck, K. Van Gasse,
  B. Kuyken, *Opt. Express* 29, 15013–15022 (2021).
- F. Kärtner, D. Zumbühl, N. Matuschek, *Phys. Rev. Lett.* 82, 4428–4431 (1999).
- 33. U. Keller, R. Paschotta, Ultrafast Lasers (Springer, 2021).
- 34. A. E. Siegman, Lasers (University Science Books, 1986).

- 35. H. A. Haus, IEEE J. Sel. Top. Quantum Electron. 6, 1173-1185 (2000).
- Q. Guo, data and computer code for "Ultrafast mode-locked laser in nanophotonic lithium niobate", version 2, Figshare (2023); https://doi.org/10.6084/m9.figshare.24208434.
- G. P. Agrawal, N. A. Olsson, IEEE J. Quantum Electron. 25, 2297–2306 (1989).
- A. Uskov, J. Mork, J. Mark, IEEE J. Quantum Electron. 30, 1769–1781 (1994).
- S. Schmitt-Rink, D. S. Chemla, D. A. Miller, *Phys. Rev. B Condens. Matter* 32, 6601–6609 (1985).

## **ACKNOWLEDGMENTS**

The device nanofabrication was performed at the Kavli Nanoscience Institute (KNI) at Caltech. The authors thank K. Vahala for loaning equipment. Q.G. thanks M.Xu for the helpful discussions. **Funding:** The authors acknowledge support from ARO grant no. W911NF-23-1-0048, NSF grant nos. 1846273 and 1918549, AFOSR award FA9550-23-1-0755, and NASA JPL. The authors thank NTT Research for their financial and technical support. **Author contributions:** Q.G. and A.M. conceived the project. Q.G. fabricated the devices with assistance from R.S. Q.G. performed the measurements and numerical simulation. R.S., J.W., B.K.G., R.M.G., L.L., L.C., and S.Z. assisted with the measurements. B.K.G., R.M.G., A.R., and M.L. helped with the numerical simulation and data analysis. Q G. wrote the manuscript with input from all authors. A.M. supervised the project.

Competing interests: Q.G. and A.M. are inventors on a patent application (US patent application no. 17/500,425) that covers the concept and implementation of the actively MLL in this work. LLL and A.M. are involved in developing photonic integrated nonlinear circuits at PINC Technologies Inc. LL. and A.M. have an equity interest in PINC Technologies Inc. The remaining authors declare no competing interests. Data and materials availability: All data are available in the manuscript or the supplementary materials. The data files supporting the plots in the main text and the computer code for simulating the MLL are available at Figshare (36). License information: Copyright © 2023 the authors, some rights reserved; exclusive licensee American Association for the Advancement of Science. No claim to original US government works. https://www.science.org/about/science-licenses-journal-article-reuse

## SUPPLEMENTARY MATERIALS

science.org/doi/10.1126/science.adj5438 Materials and Methods Supplementary Text Figs. S1 to S9 Tables S1 and S2 References (40–48)

Submitted 2 July 2023; accepted 4 October 2023 10.1126/science.adj5438